

Time-dependent states in the Weissenberg effect

Michael M. Degen, William J. Kahle, and C. David Andereck

Department of Physics, The Ohio State University, 174 West 18th Avenue, Columbus, Ohio 43210

(Received 3 October 1997)

Experiments characterizing time-dependent states in the Weissenberg effect in First Brand Corporation's STP™ oil additive are described. The Weissenberg effect is the climbing of a rotating rod by a viscoelastic fluid. The results of a general survey of the states found with varying rod diameter, fluid height, and fluid temperature are presented. A detailed examination is made of the sequence of states found with a particular rod diameter and fluid depth. In this case, the Weissenberg effect is shown to exhibit characteristics of the Ruelle-Takens route to chaotic flow. In this case, the flow undergoes successive bifurcations from a time independent state to states with one frequency, two frequencies, three frequencies and then chaos, characteristic of the Ruelle-Takens route to chaos. [S1063-651X(98)13202-6]

PACS number(s): 47.52.+j, 83.50.Eb, 47.50.+d, 61.25.Hq

I. INTRODUCTION

Non-Newtonian fluids can be found throughout nature, including everyday examples such as mayonnaise, ketchup, and paints. Even though these fluids are quite common, much of their flow behavior remains undocumented. Many heuristic models have been proposed to describe the wide variety of non-Newtonian fluids. (Examples of these models can be found in rheology texts such as that of Macosko [1]).

While some of the models fit some of the data quite well, no particular model stands out as correct under all circumstances. Some of the models appear to violate fundamental laws of physics. For example, the so-called second-order model term (proportional to the square of the velocity gradi-

ent), which is used to describe some viscoelastic fluids, has been shown to drop out of the stress tensor after consideration of symmetry and the laws of thermodynamics [2], leaving only the Newtonian term, which is insufficient to describe the observed phenomenon. It has been suggested by Brand [2] that a detailed examination of the Weissenberg effect in particular may aid in showing where these second-order models break down and possibly inspire a better model of some non-Newtonian fluids.

The Weissenberg effect (so called based upon his pioneering experiments on the phenomenon [3]) occurs when a non-Newtonian fluid climbs up a rotating rod immersed in a pool of the fluid. Whether the fluid climbs at all, or to what extent, depends on its exact nature. In particular, the fluid must have

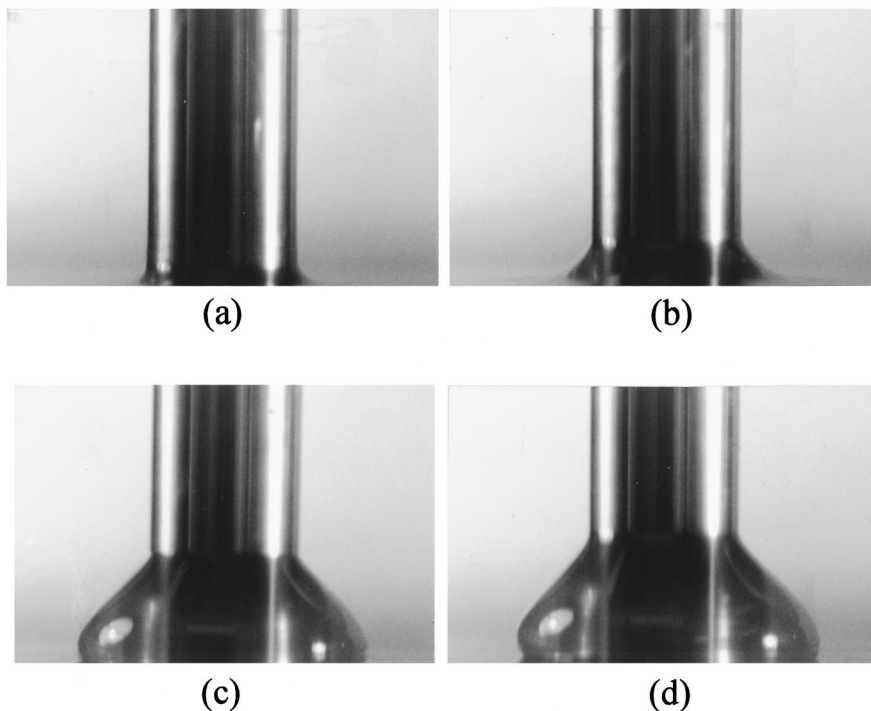


FIG. 1. Side view of the Weissenberg effect in STP™ with $d_r=1.27$ cm, $h=2.7$ cm, and $T=20$ °C. (a) Wetting meniscus at $F=0.0$ rev/sec, (b) concave shape at $F=1.0$ rev/sec, (c) convex shape with cusp at the surface of the bulk fluid at $F=3.0$ rev/sec, and (d) broken axial symmetry at $F=3.5$ rev/sec (at this point in the rotation cycle the bulge is greater on the right than on the left).

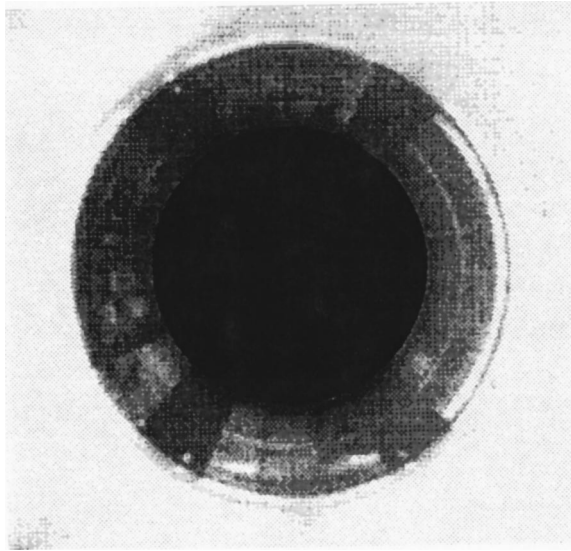


FIG. 2. Top view of the Weissenberg effect in STP™ at $F = 2.0$ rev/sec showing the axisymmetric climbing fluid. The circle at the center of the picture is the top of the rod with $d_r = 1.27$ cm.

elastic properties. Representative side views of this effect appear in Fig. 1, while top views are shown in Figs. 2 and 3.

A theoretical analysis of the Weissenberg effect and a corresponding series of experiments have been performed by Joseph and numerous colleagues [4–11]. A summary can be found in Joseph's book [12]. Studies of the bulk flow in the fluid have been performed by Eitelberg [13,14]. All of these authors concentrated on the primary states at low rod rotation rates and only briefly mention the existence of time-

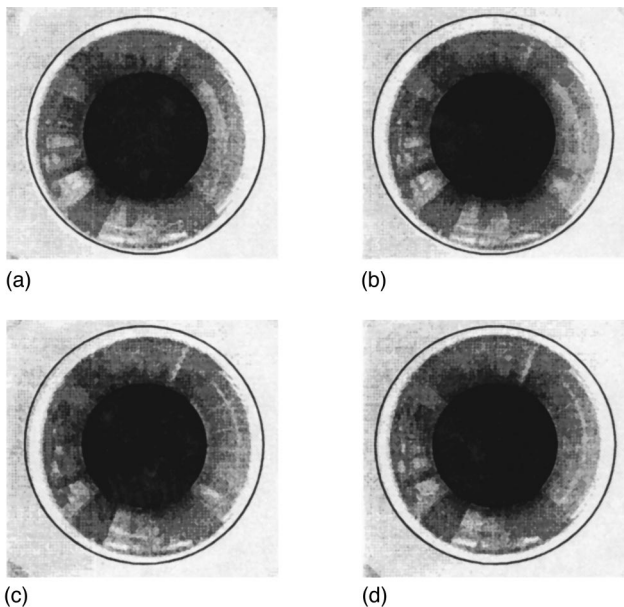


FIG. 3. Sequential top views of the Weissenberg effect in STP™ at $F = 2.3$ rev/sec showing the broken axial symmetry, captured every 0.3 sec. The circle at the center of each picture is the top of the rod, with $d_r = 1.27$ cm. The larger circle is concentric with the rod to serve as a reference. The climbing fluid is shown extending (a) toward the bottom left, (b) toward the bottom right, (c) toward the top right, and (d) toward the top left.

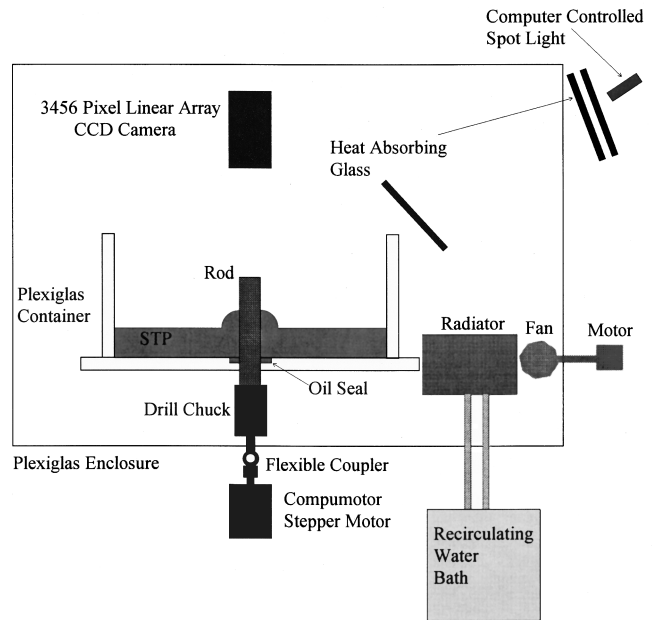


FIG. 4. Schematic diagram of the Weissenberg apparatus.

dependent states at higher rod rotation rates, which we examine in detail in this paper.

This paper is organized as follows. In Sec. II we describe the apparatus. Section III describes the experimental procedure and data analysis. Section IV discusses the experimental results. Section V contains our conclusions.

II. APPARATUS

A schematic diagram of the apparatus used in these experiments is shown in Fig. 4. The design of the apparatus took into account the desire to observe the climbing fluid from all angles. The container is made from a 30.5-cm-diam Plexiglas cylinder bonded to a Plexiglas plate that serves as the bottom. The rod enters the container from below, leaving the top open for visualization. A precision drill chuck holds the rod in place and is supported by bearings. This method of supporting the rod was chosen to facilitate easy changes of the rod. An aluminum disk holds an oil seal that fits snugly over the rod and is sealed flush with the bottom of the container. It should be noted that early experiments showed a localized heating due to friction between the rod and seal. A 3.2-mm Plexiglas sheet serves as a false bottom and isolates

TABLE I. Ingredients of STP™ oil treatment. Data taken from a material safety data sheet were provided by the manufacturer [19].

Material	Content (%)
Chemically neutralized heavy naphthenic petroleum distillates	15–40
Solvent-dewaxed heavy paraffinic petroleum distillates	60–80
Zinc dialkyldithiophosphate	3–11
Calcium sulfonate	1–4
Amine grafted ethylene-propylene copolymer	3–11

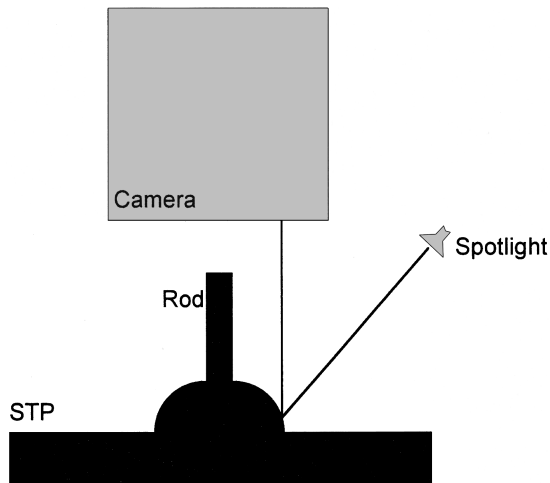


FIG. 5. Diagram showing the lighting scheme.

the fluid from the aluminum disk. Subsequent temperature measurements have shown this to virtually eliminate the problem. A flexible coupler is used to connect the drill chuck to a Compumotor™ stepper motor model A/AX83-93, which drives the rod into rotation at a rate F . The motor is driven by a Compumotor™ AX Series controller. The rods are made out of commercially available drill rod, which has a precisely ground radius. Three rods were used with diameters (d_r) 0.64, 0.95, and 1.27 cm.

Initial survey investigations used visualization from the

side with an area scan charge coupled device (CCD) camera. Images were captured on a video cassette recorder.

Subsequent measurements used visualization of the climbing fluid from above with a Loral Fairchild 3456 pixel linear array CCD camera. The CCD camera is interfaced to a computer via a MuTech MV-1000/1100 image acquisition board. Illumination of the climbing fluid is with a standard 50-W halogen spotlight. The spotlight is turned on and off via a relay switch controlled through the computer's parallel port. This allows a minimum amount of thermal radiation from the bulb to be introduced into the system. Additionally, three sheets of heat (infrared radiation) absorbing glass are positioned along the light path to further reduce the heating of the fluid.

The apparatus is contained inside a Plexiglas box for temperature control. Constant temperature water is circulated through a radiator. A fan circulates the air inside the box past the radiator. A thermistor is immersed in the fluid to measure the temperature. The resistance of the thermistor is monitored by a Hewlett-Packard 3478A DMM, which is interfaced to the computer via the GPIB interface bus. It should be noted that all heat sources, including the driving motor, the fan motor, and the light bulb, are outside the containment box. The temperature controlled water is provided by a Brinkmann Instruments Lauda RM6 recirculating temperature bath.

The selection of the fluid was driven by two considerations. First, the fluid should be readily available. Second,

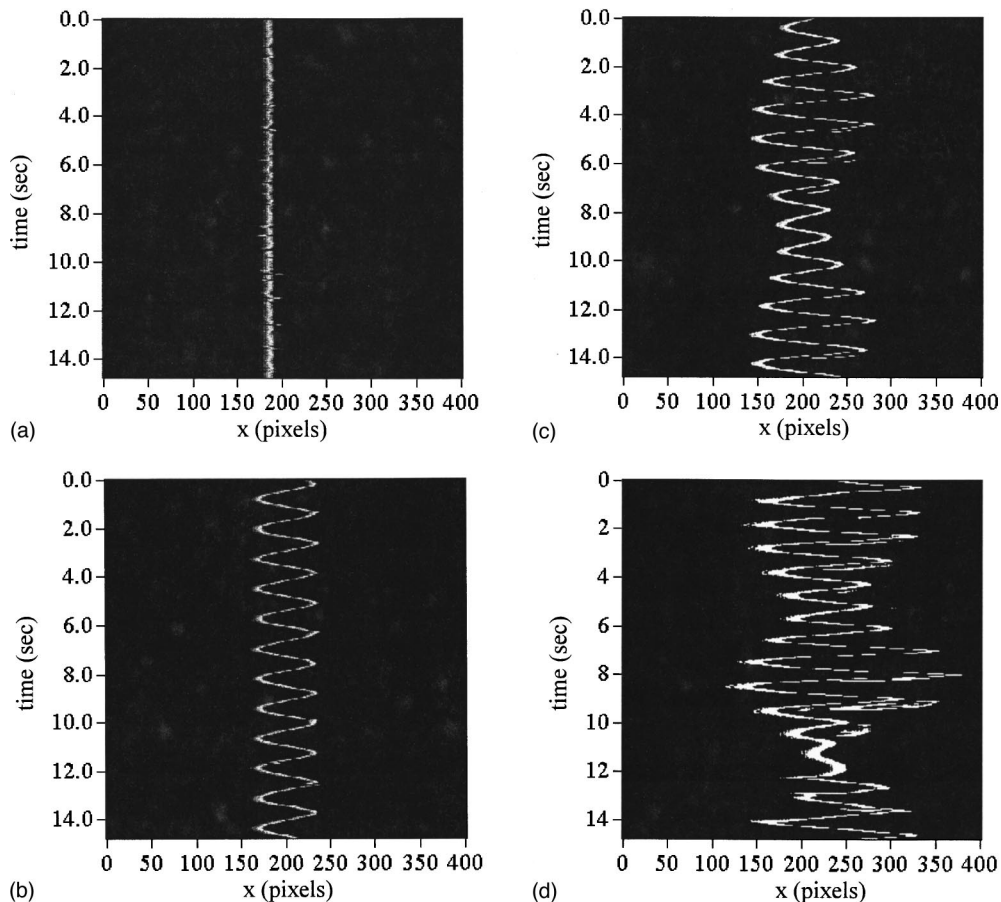


FIG. 6. Gray-scale images of raw data at $T=16.6^\circ\text{C}$. Captured at (a) $F=1.769$, (b) $F=1.899$, (c) $F=2.015$, and (d) $F=2.510$ rev/sec.

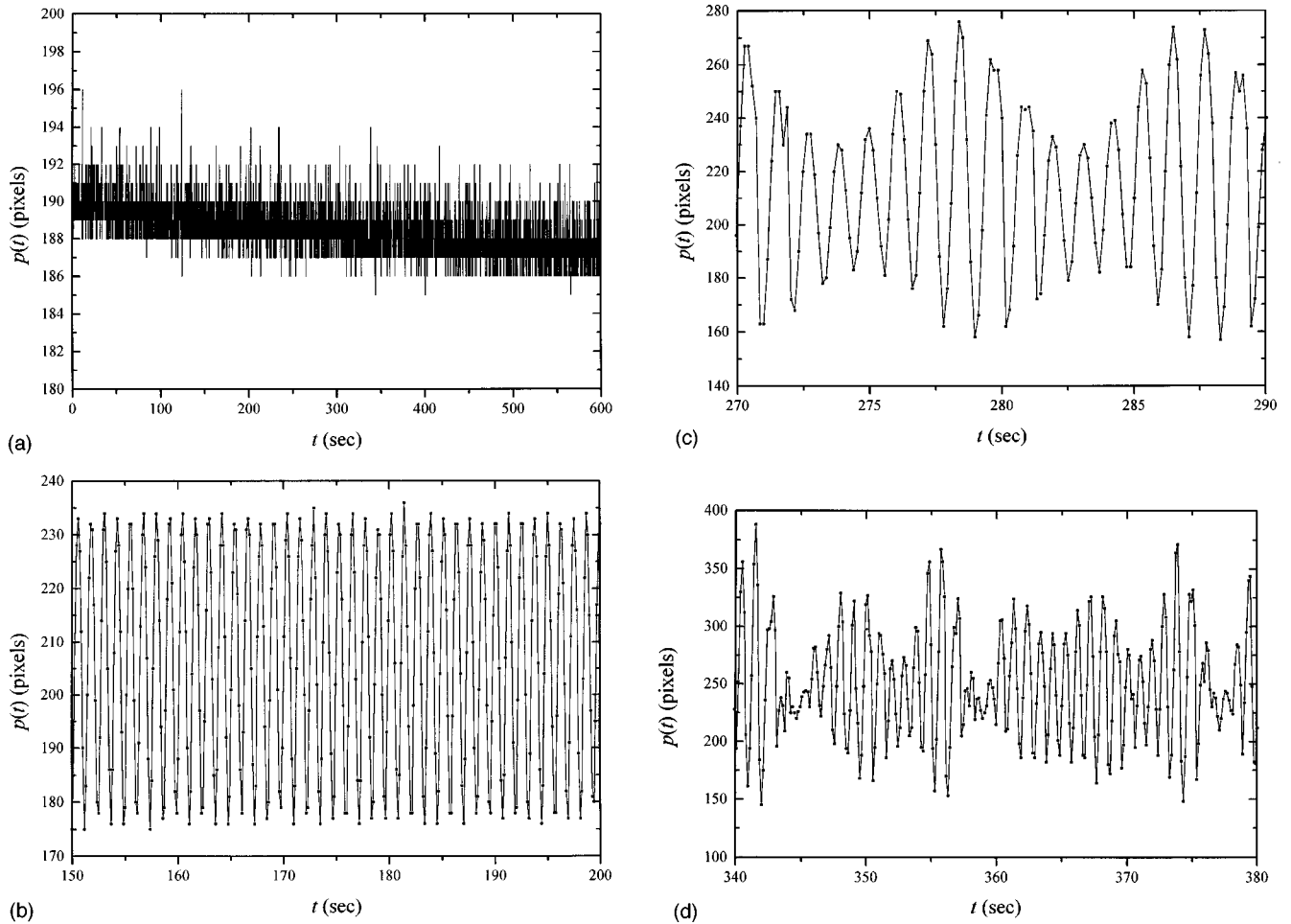


FIG. 7. Position of the edge of the climbing fluid from (a) Fig. 6(a), (b) Fig. 6(b), (c) Fig. 6(c), and (d) Fig. 6(d).

there is a desire to recreate previous experimental conditions to calibrate the apparatus. To this end, we follow the lead of Joseph *et al.* [5,7,8] in choosing First Brand Corporation's STP™ Oil Treatment. STP™ is sold as a viscosity index improver for automobile engines. While the exact content of STP™ is a trade secret, the main ingredients are listed in Table I. Characterization of STP™ in terms of the constitutive constants of second-order fluids can be found in [7,15] and references therein.

III. EXPERIMENTAL PROCEDURE AND DATA ANALYSIS

The initial steps include filling the system with STP™ to the desired height (h), starting the temperature control and waiting ~ 12 h for temperature stabilization. Once the initial equilibration period has passed, a data run can be initiated. A data run using side visualization consists of systematically increasing the rod rotation rate (F) from 0 to 15 rev/sec over a period of ~ 5 h. F is increased in steps of 0.08 or 0.1 rev/sec with a typical waiting period of ~ 100 sec between steps.

Analysis of the video tape data is performed manually. A time stamp on the video tape is correlated with information from the motor controlling computer to determine F .

A data series using the 3456-pixel linear array camera begins at a value of F below the onset to the time-dependent

state. Once the desired value of F is set, the system is maintained at this value for ~ 1 h, following which a data file is collected. Data files typically consist of 32 768 lines taken at time intervals of $\delta t = 0.00922$ sec between the lines. Each line is usually 400 pixels wide. After the data set is captured, F is increased by $\delta F \approx 0.01$ rev/sec or less and the waiting period initiated. The data series typically ends when the climbing fluid has started to exhibit chaotic time dependence.

A data series from the linear array camera concentrates on characterizing the time dependence of the climbing fluid. The first step in this process is to determine the position of the edge of the climbing fluid as a function of time $p(t)$. Once $p(t)$ is known, standard techniques such as power spectral analysis and the construction of return maps can be used to characterize the phenomena.

Determining the edge of the climbing fluid depends primarily on the nature of the original data file. The method chosen here is to illuminate the climbing fluid from an angle such that only light from the edge of the climbing fluid enters the camera, as shown in Fig. 5. Therefore, the raw data set shows a line of high intensity indicating the edge of the climbing fluid in a dark background, as shown in Fig. 6.

Once the data sets have this form, the next task is to determine the position of the edge of the climbing fluid. Through trial and error, a procedure of averaging three spatial pixels and four sequential lines and comparing to an

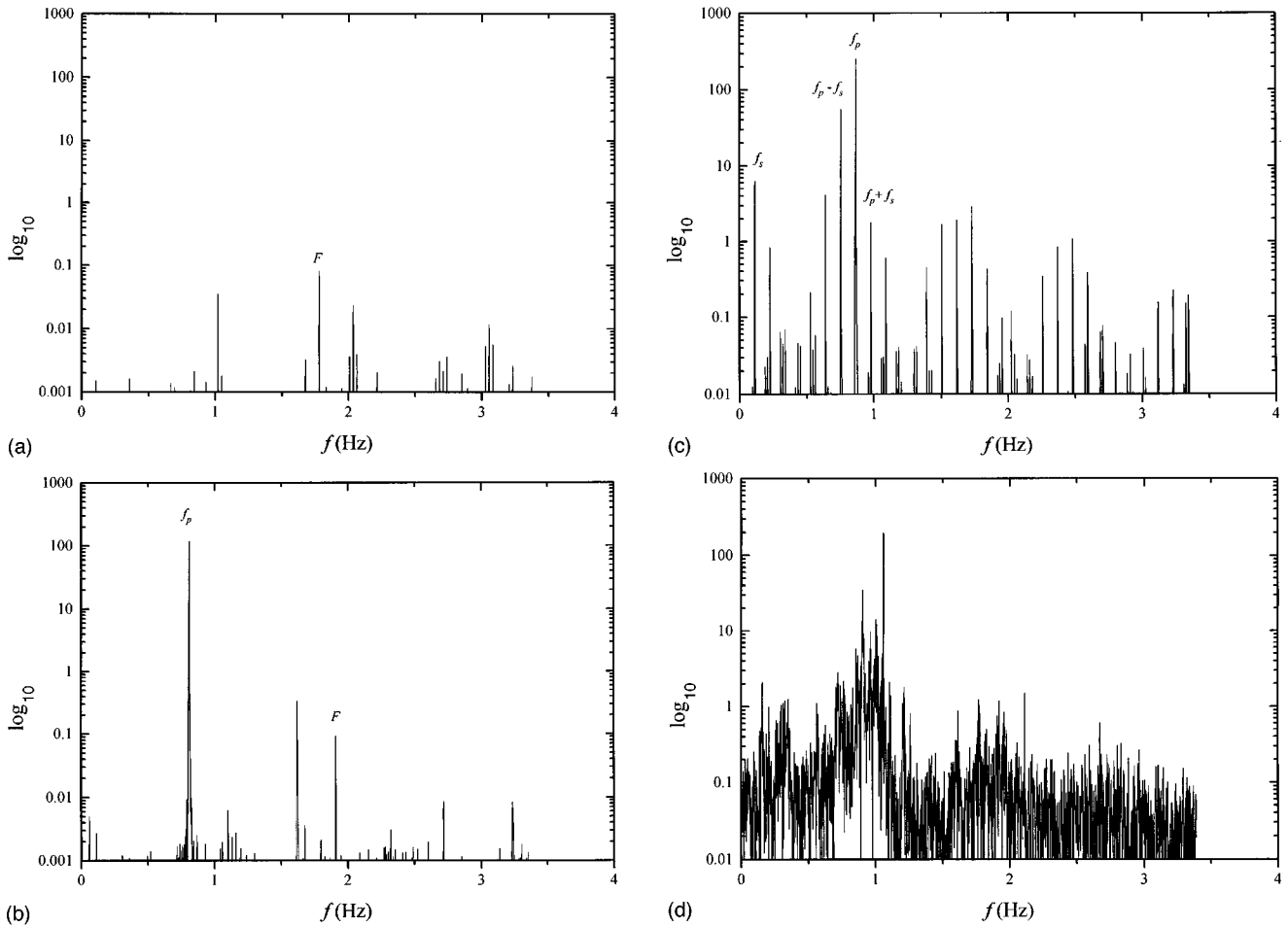


FIG. 8. Power spectra corresponding to (a) Fig. 7(a), (b) Fig. 7(b), (c) Fig. 7(c), and (d) Fig. 7(d).

arbitrary cutoff was finally settled upon. This averaging scheme reduces the file from 32 768 lines to 8192 positions of the edge of the climbing fluid $p(t)$. Examples of the output from this program can be seen in Fig. 7.

Once $p(t)$ has been found, a fast-Fourier-transform technique is used to determine the power spectrum. The power spectrum routine is from Ref. [16]. Examples of power spectra can be seen in Fig. 8. The power spectra are then analyzed to determine the dominant frequencies present in the flow.

In addition to power spectra, the edge of the climbing fluid data is analyzed using return maps. Return maps are produced by mapping time series data onto a coordinate system of (x, y, z) as $(p(t), p(t + \delta t), p(t + 2\delta t))$, where δt is



FIG. 9. Side view of the nautilus mode with $d_r = 1.27$ cm, $h = 0.7$ cm, $T = 20$ °C, and $F = 5.5$ rev/sec. A strong shape asymmetry is visible in this view.

the time delay. Following Abarbanel [17], the time delay is chosen as the δt at the first minimum of the “average mutual information.”

Return maps can be quite complicated even with the best

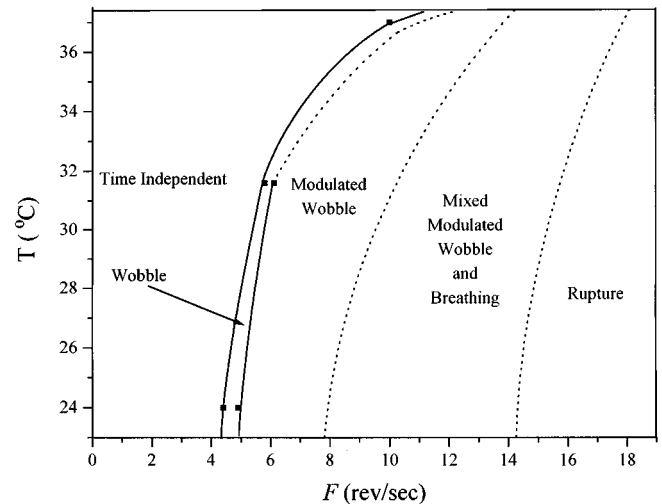


FIG. 10. Phase diagram for the Weissenberg effect in STP™ with $d_r = 0.64$ cm and $h = 2.5$ cm. Solid lines represent stability boundaries and are drawn to guide the eye. Dotted lines are approximate stability boundaries that are more difficult to determine visually.

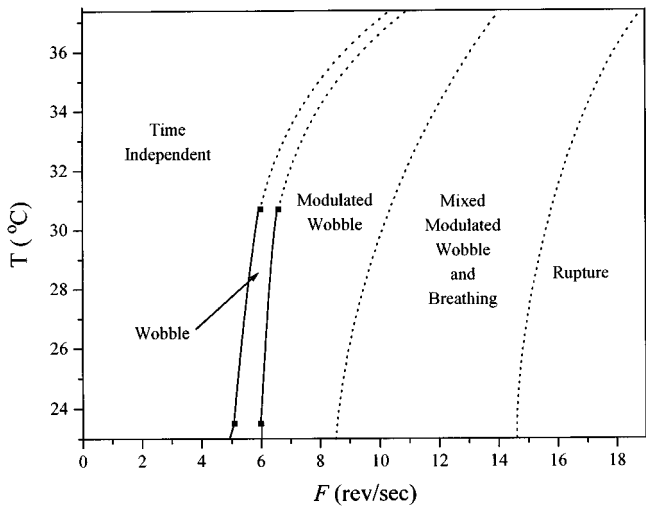


FIG. 11. Phase diagram for the Weissenberg effect in STP™ with $d_r=0.95$ cm and $h=2.5$ cm. Solid lines represent stability boundaries and are drawn to guide the eye. Dotted lines are approximate stability boundaries that are more difficult to determine visually.

δt . A Poincaré section is used to reduce the level of complexity of a high-dimensional map. For a discussion of Poincaré sections see Ref. [18].

Operationally, the return maps are calculated from $p(t)$ using the following procedure. The first step in this process is to subtract out the average of $p(t)$, yielding $p(t) - \langle p \rangle$. This step merely shifts the $p(t)$ from oscillating around some unknown value to oscillating around 0. Since the data are oscillating around zero, the Poincaré section is chosen to be the $z=0$ plane. The next step in the process is to determine when the trajectory has crossed the plane, i.e., find when $z(i) < 0$ and $z(i+1) > 0$. Once this is known a FORTRAN [16] routine is used to interpolate the point $(x, y, 0)$ from the trajectory. Five points along the trajectory are fit with a fourth-

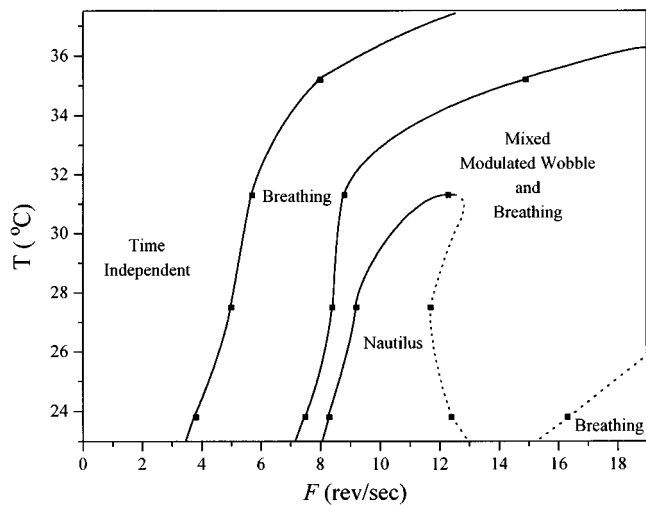


FIG. 12. Phase diagram for the Weissenberg effect in STP™ with $d_r=1.27$ cm and $h=0.7$ cm. Solid lines represent stability boundaries and are drawn to guide the eye. Dotted lines are approximate stability boundaries that are more difficult to determine visually.

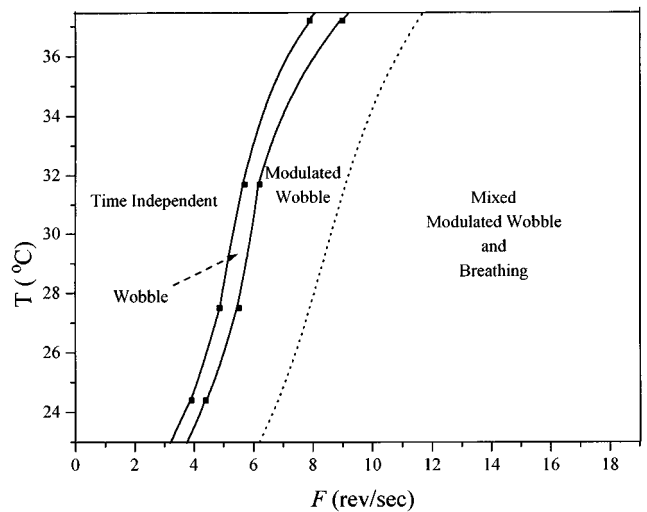


FIG. 13. Phase diagram for the Weissenberg effect in STP™ with $d_r=1.27$ cm and $h=1.7$ cm. Solid lines represent stability boundaries and are drawn to guide the eye. Dotted lines are approximate stability boundaries that are more difficult to determine visually.

order polynomial for this task. Once the point is found, this process is repeated for other points along the trajectory.

IV. EXPERIMENTAL RESULTS

A. General survey

The initial phase of the investigation employed side visualization. A general survey of the states found with different rod diameters, fluid heights, and fluid temperatures has been performed.

The states at low F are time independent and have been studied extensively by Beavers and Joseph [5,6,8-10]. At

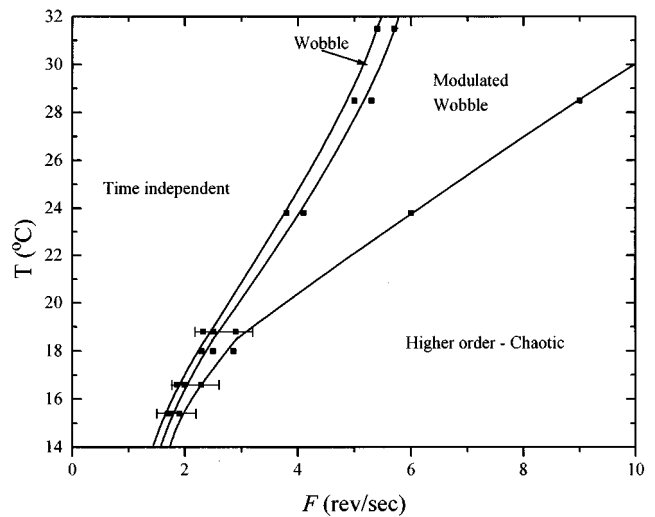


FIG. 14. Phase diagram for the Weissenberg effect in STP™ with $d_r=1.27$ cm and $h=2.7$ cm. Solid lines represent stability boundaries and are drawn to guide the eye. Horizontal lines indicate the range of detailed investigation described in Sec. IV B in the text.

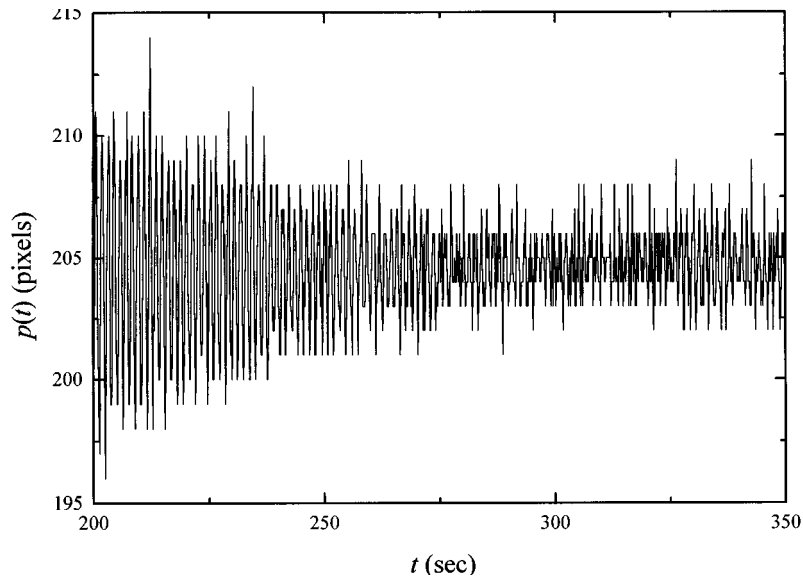


FIG. 15. Position of the climbing fluid just at the onset to the primary mode ($F=1.839$ rev/sec) showing a decrease in the amplitude with time.

higher F , the climbing fluid begins to exhibit various time-dependent modes. The first is the “wobble,” which breaks the axial symmetry as shown in Figs. 1(d) and 3. A second state is the “modulated wobble.” These two states will be discussed in detail below.

Other time-dependent modes include breathing, nautilus, and rupture. Breathing, as observed by Joseph [7], is an axisymmetric rising and falling of the free surface of the climbing fluid parallel to the axis of the rod. The nautilus mode is an asymmetric wobble-like structure with a spiral tail near the bulk fluid surface (see Fig. 9). Finally, at high F , the rupture mode results in fluid being thrown around the container away from the rod, apparently in a random fashion.

The results of the general survey are shown in a series of phase diagrams, Figs. 10–14. Several general features are evident from these phase diagrams. First, the size of the rod has less effect on the transition to the first time-dependent state than on the secondary transitions. Next, the transition from time independent to wobble to modulated wobble is

generic for all rod sizes, provided the fluid height is sufficient. This is consistent with previous observations by Eitelberg [14]. Finally, the more exotic time-dependent states appear with small fluid heights.

B. Detailed examination for $d_r=1.27$ cm and $h=2.7$ cm

The time-dependent states with rod diameter 1.27 cm and fluid depth 2.7 cm (Fig. 14) have been investigated in detail at various temperatures. The rotation rate scan ranges are indicated in Fig. 14 as well.

The acquisition procedure described above yields a series of data files at increasing values of the rod rotation rate F . Analysis of these files consists of, first, finding the position of the climbing fluid $p(t)$, second, finding the power spectrum, and, finally, finding the Poincaré sections. $p(t)$ and the power spectra are used to determine the onset of the primary (wobble) f_p and secondary (modulated wobble) f_s mode fre-

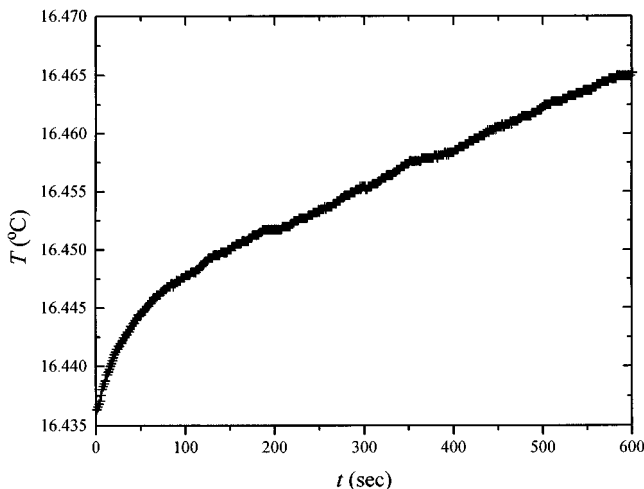


FIG. 16. Temperature of the fluid during the capture of the data file shown in Fig. 15.

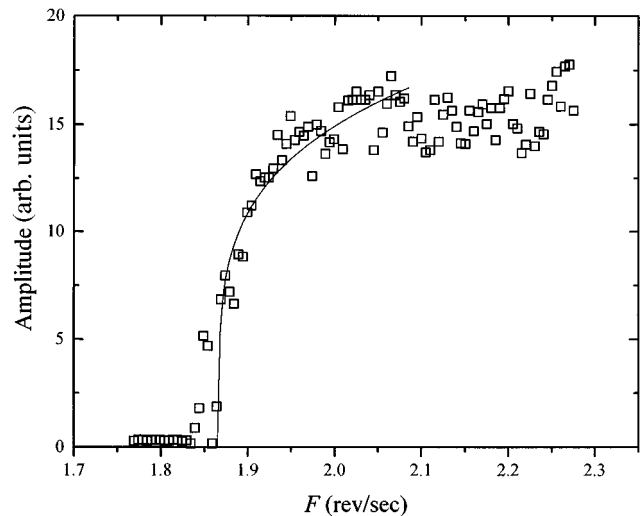


FIG. 17. Amplitude of f_p vs F at $T=16.6$ °C. The solid line is a fit with Eq. (1), where $\alpha=0.22$.

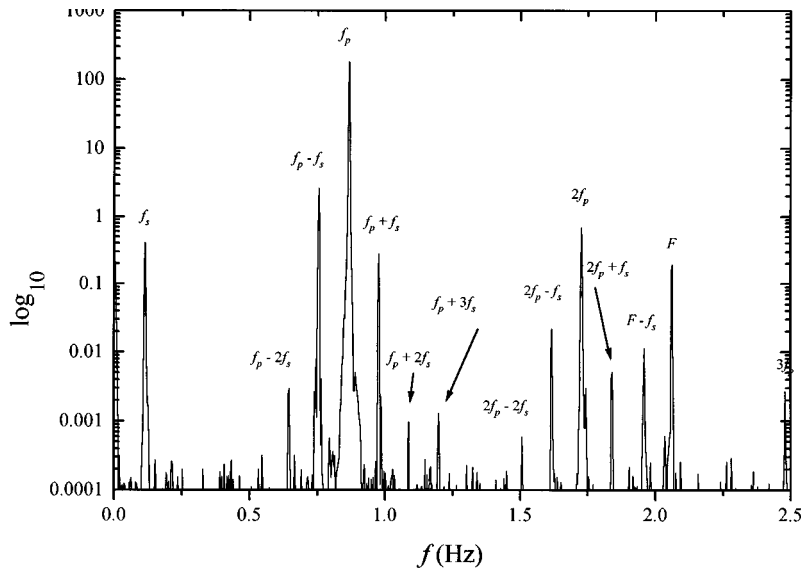


FIG. 18. Power spectrum at $F=2.049$ rev/sec at $T=16.6$ °C with all of the peaks identified.

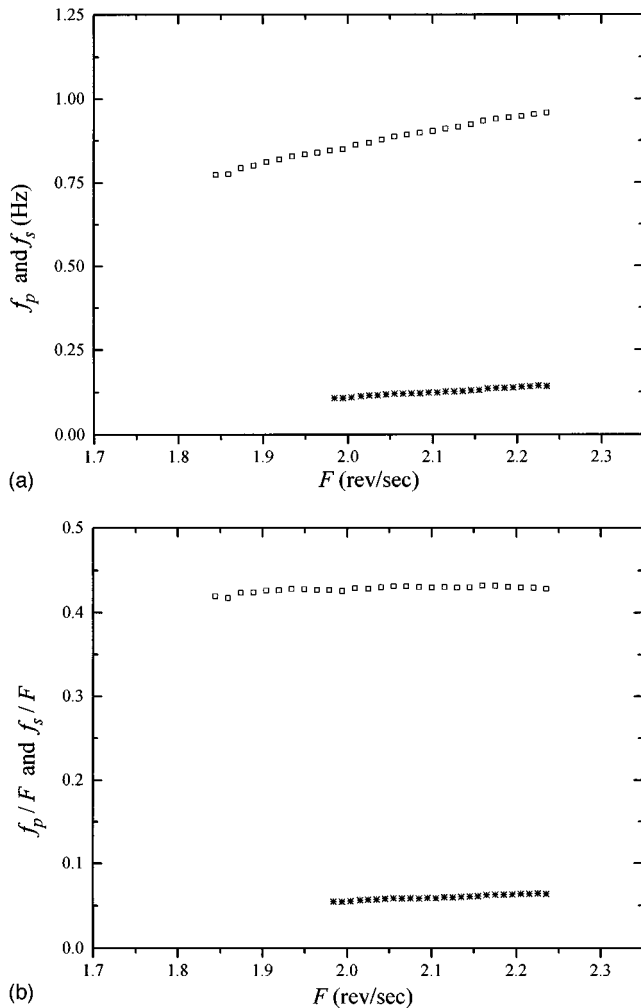


FIG. 19. (a) Primary f_p and secondary f_s frequencies vs rotation rate F at $T=16.6$ °C. (b) Same frequencies plotted as ratios to F .

frequencies. The onset rod rotation frequency values are labeled F_p and F_s , respectively. In addition, the power in each frequency can also be found.

Analysis of $p(t)$ and the power spectra for $F < F_p$ shows an extremely small time dependence at the frequency $f = F$ [see Figs. 7(a) and 8(a)]. This shows that the rod is not perfectly aligned, but is very close. The plot of $p(t)$ at $F \cong F_p$ shows the onset to the wobble but with a decrease in the amplitude with time as in Fig. 15. The corresponding power spectrum shows the emergence of the primary mode frequency f_p . Investigation of this decaying amplitude led us to monitor the temperature of the fluid during the acquisition of the data file, as plotted in Fig. 16. The temperature of the fluid rises ~ 0.03 °C during the data capture routine. This temperature rise seems to be the only source for the decrease in the amplitude of the wobble. The next data file in the series, at slightly higher F , shows a strong wobble with a consistent amplitude over the complete file.

The temperature dependence of F_p can be clearly shown by capturing a series of data sets at different temperatures. Analysis shows the temperature dependence of F_p as plotted in Fig. 14. Higher STP™ temperatures require higher F_p for the onset to the primary mode. This supports the idea that the decaying amplitude observed at $F \cong F_p$ is due to a slight increase in the temperature.

Above the onset of the primary oscillatory mode but below the onset of the secondary ($F_p < F < F_s$), the wobble is clearly evident [see Fig. 7(b)]. Analysis of the power spectra [Fig. 8(b)] shows that the amplitude of the primary frequency increases from zero with increasing F as in Fig. 17. Attempts to fit the amplitude of the primary mode of a number of data sets with

$$A \propto (F - F_p)^\alpha \tag{1}$$

show a range of $\alpha \sim 0.1 - 0.4$, with a typical fit shown in Fig. 17.

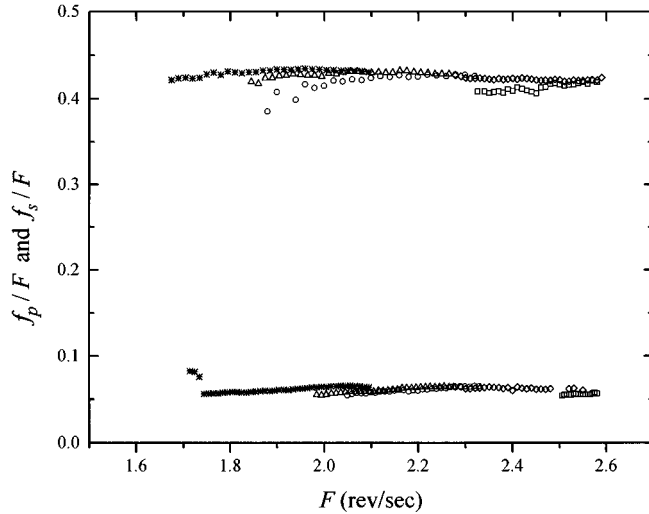


FIG. 20. Ratio of the primary and secondary frequencies to F (f_p/F and f_s/F) vs F from different data sets at $T=15.4$ °C (*), $T=16.6$ °C (Δ), $T=16.6$ °C (\diamond), $T=16.6$ °C (\circ), and $T=18.8$ °C (\square). Sets at the same temperature were taken at different times to show reproducibility.

At $F=F_s$, a second frequency f_s enters the system as a modulation on top of the primary [see Figs. 7(c) and 8(c) in which the variation of the wobble amplitude with time is shown). A plot of F_p and F_s vs temperature appears as a phase diagram for the system in Fig. 14. f_s is incommensurate with f_p . Many other peaks also appear in the power spectrum at F_s . Two of the largest are the sum peak at $f_p + f_s$ and the difference peak at $f_p - f_s$. A power spectrum with all of the peaks identified can be seen in Fig. 18. A plot of f_p and f_s vs F for one data set is shown in Fig. 19(a). This plot shows a linear increase in both f_p and f_s with F . Perhaps a more revealing graph can be found in Fig. 19(b), which shows f_p/F and f_s/F vs F . This shows $f_p/F=0.42$ and $f_s/F=0.061$ independent of F .

Combining the plots of f_p/F and f_s/F vs F from different data sets yields the plot in Fig. 20. As can be seen, the ratios f_p/F and f_s/F are nearly identical regardless of the

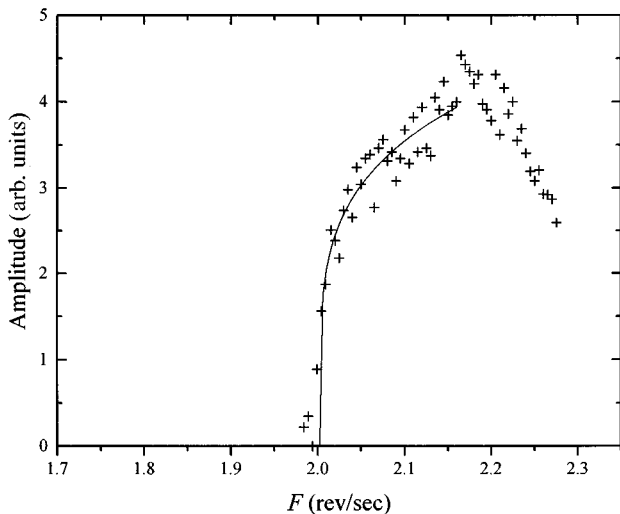


FIG. 21. Amplitude of the secondary mode at $T=16.6$ °C. The solid line is a fit with Eq. (1), where $\alpha=0.21$.

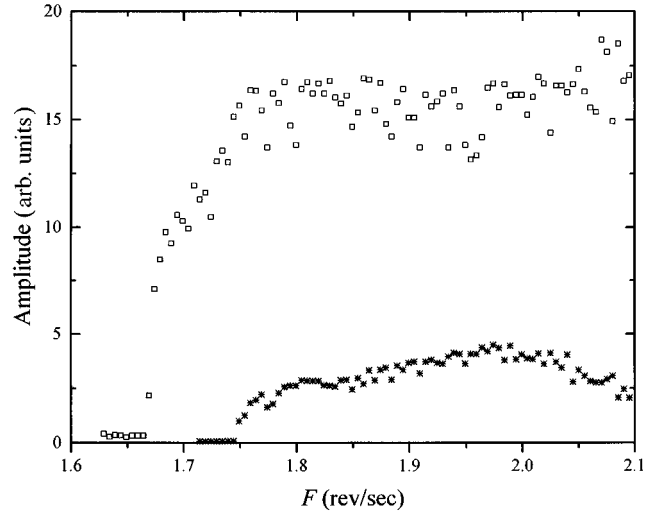


FIG. 22. Amplitudes of both the primary (\square) and secondary (*) modes at $T=15.4$ °C.

particular data set or the temperature of the STPTM. Data sets taken with decreasing F show similar results. No hysteresis has been observed within our resolution.

In addition to the frequencies, the amplitude of the secondary mode has also been analyzed. Figure 21 shows this amplitude vs F . Like the primary, the secondary grows in amplitude from zero with increasing F , until higher-order modes enter into the flow, at which point the amplitude begins to drop ($F \sim 2.15$ rev/sec). However, a comparison of the primary and secondary amplitudes shows that the latter is always significantly smaller than the former (Fig. 22). Attempts to fit Eq. (1) to the amplitude of the secondary show a range of $\alpha=0.2-0.4$ for various data sets, with a typical fit in Fig. 21.

There is some evidence of a third frequency entering the motion at rod rotation rates above the onset to the secondary mode ($F > F_s$) (see Fig. 23). However, the peak in the power spectrum exists only for a very short range in F and quickly splits into two new peaks (at higher F). More detailed study is needed to identify the physical feature corresponding to this elusive third frequency.

Upon further increases in F , $p(t)$ begins to exhibit chaotic characteristics. The power spectra show significant increases of the power in the harmonics relative to the power in the primary frequencies. Additionally, a broadband background begins to appear [Fig. 7(d)]. More discussion of the chaotic nature of the flow will appear in the following section.

Poincaré sections

The Poincaré sections for data files with $F < F_p$ are small dots at (0,0) since the value of $p(t) - \langle p \rangle$ is essentially zero. At $F_p < F < F_s$, the points on the Poincaré section move away from (0,0) and the spot grows as in Fig. 24(a). The ideal Poincaré section for this single-frequency time series would be a single point located at some value (x,y) . Since there is some noise in the experimental $p(t)$, the single point is smeared out into a finite-sized spot.

At $F=F_s$, the Poincaré section expands and begins to show a more complex structure [Fig. 24(b)]. Increasing F

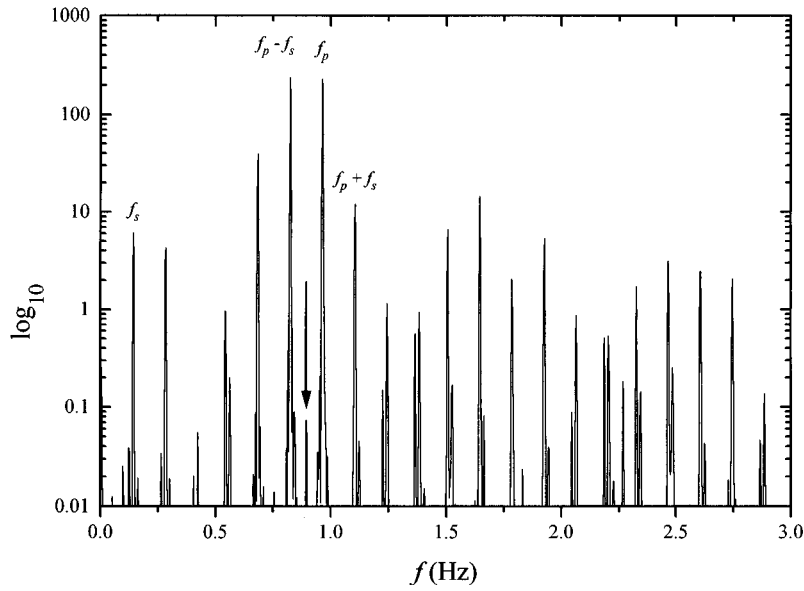


FIG. 23. Evidence of a third frequency (identified with the arrow) entering the motion. Data were taken for $F=2.059$ rev/sec at $T=16.6^\circ\text{C}$.

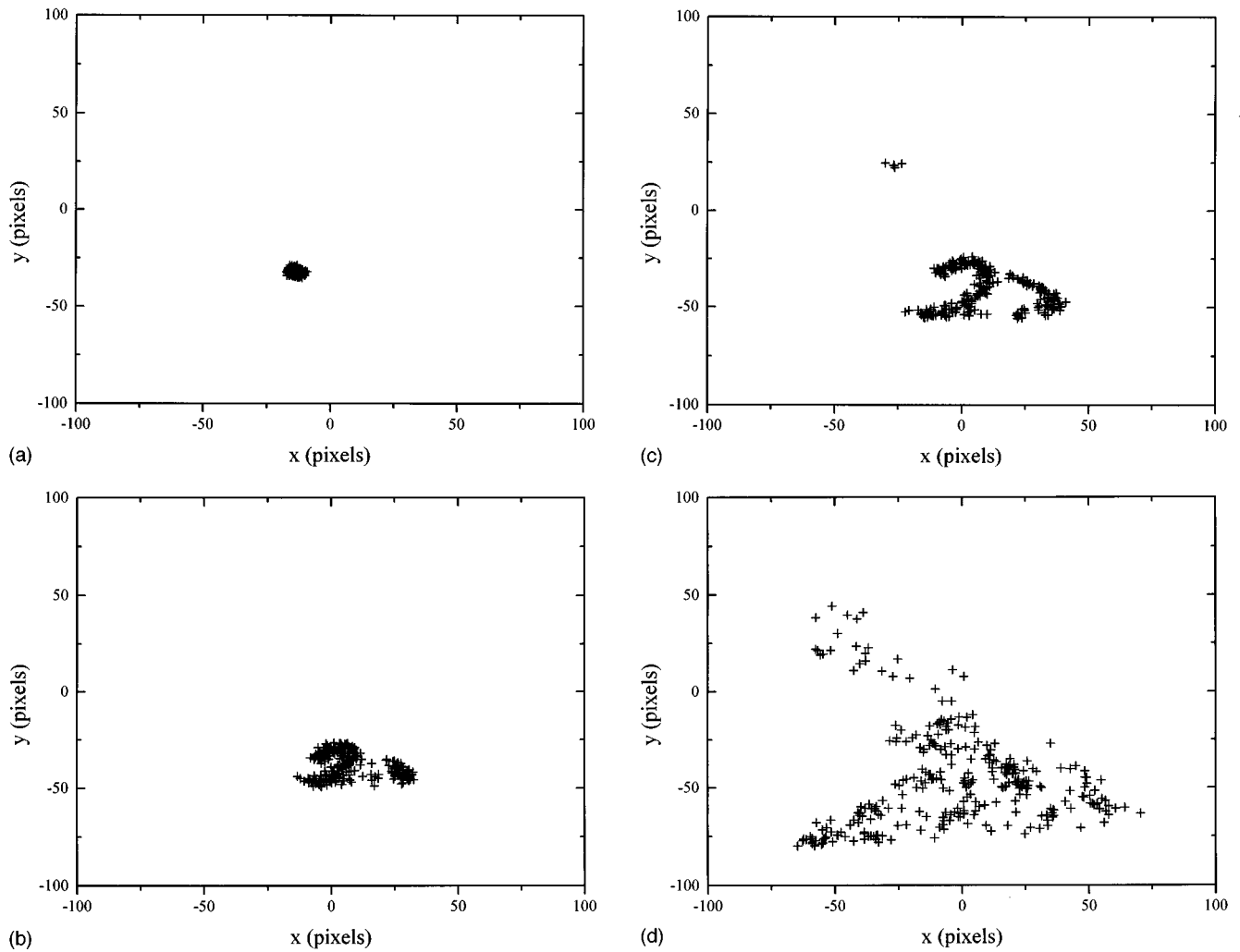


FIG. 24. Poincaré sections at $T=16.6^\circ\text{C}$ for (a) $F=2.029$ rev/sec, above the onset to the wobble but below the modulation, (b) $F=F_s=2.059$ rev/sec, (c) $F=2.089$ rev/sec, and (d) $F=2.329$ rev/sec showing a chaotic state.

above F_s (but below the more chaotic region) shows Poincaré sections as in Fig. 24(c). The area covered by points has expanded, but definite structure is still evident. The Poincaré section continues to fill more of the space at still higher F [Fig. 24(d)]. Some structure is still evident, indicating that the flow is not random, but rather chaotic in nature.

V. CONCLUSION

The Weissenberg effect (rod climbing) has been studied in First Brand Corporation's STP™ oil additive. A survey of the states found with varying rod diameter, fluid height, and temperature has been performed. This survey shows that the rod diameter has little effect on the primary transitions. However, the height of the fluid changes the observed states if h is less than the rod diameter.

The transitions from a steady state to a time-dependent state with one frequency, two frequencies, and more have been identified and characterized as a function of rod rotation rate F and at various temperatures of the fluid. The onset rotation rate F_p to the primary frequency increases with increasing temperature. The value of the ratio of the primary frequency to the rotation rate $f_p/F=0.42$ is independent of the temperature and F . The amplitude of the primary frequency increases with F .

A second frequency (f_s) enters the motion at a rod rotation rate of $F_s > F_p$. Like the primary frequency, the ratio of the frequency of the secondary mode to F is also independent of temperature and F with a value of $f_s/F=0.061$.

There is some evidence suggesting the existence of a third frequency. However, further work needs to be done to conclusively identify it.

At still higher values of F , a broadband background begins to appear in the power spectra. This broadband background signals the onset of chaotic time dependence in the flow. This sequence of states, from one frequency to two frequencies to three frequencies and then chaos, is reminiscent of the Ruelle-Takens scenario. (For a discussion of the Ruelle-Takens route to chaos, see Ref. [18].) This similarity to the Ruelle-Takens scenario suggests that the Weissenberg effect behaves as a low-dimensional system with few effective degrees of freedom. Further refinement of the apparatus is necessary for direct measurement of the dimension of the system to confirm this conjecture.

In addition to the frequency, Poincaré sections have been used to characterize the flow states. The Poincaré sections support the conclusions based on the power spectra analysis of the appearance of chaotic time dependence at $F > F_s$. With this work as a basis, future investigations will focus on flows of other, simpler, and more precisely characterized fluids, with the strong possibility of modeling the behavior.

ACKNOWLEDGMENTS

The authors are grateful to H. Brand and J. Zakin for helpful discussions. W.K. was financially supported by Ohio State University.

-
- [1] C. W. Macosko, *Rheology: Principles, Measurements, and Applications* (VCH, New York, 1994).
 - [2] H. R. Brand, in *Spatio-Temporal Patterns in Nonequilibrium Complex Systems*, edited by P. E. Cladis and P. Palffy-Muhoray (Addison-Wesley, Reading, MA, 1995), pp. 211–217.
 - [3] K. Weissenberg, *Nature (London)* **159**, 310 (1947).
 - [4] D. D. Joseph and R. L. Fosdick, *Arch. Ration. Mech. Anal.* **49**, 321 (1973).
 - [5] G. S. Beavers and D. D. Joseph, *J. Fluid Mech.* **69**, 475 (1975).
 - [6] G. S. Beavers and D. D. Joseph, *J. Fluid Mech.* **81**, 265 (1977).
 - [7] D. D. Joseph, G. S. Beavers, and R. L. Fosdick, *Arch. Ration. Mech. Anal.* **49**, 381 (1973).
 - [8] D. D. Joseph and G. S. Beavers, *Arch. Ration. Mech. Anal.* **62**, 323 (1976).
 - [9] D. D. Joseph and G. S. Beavers, *Rheol. Acta* **16**, 169 (1977).
 - [10] D. D. Joseph *et al.*, *J. Rheol.* **28**, 325 (1984).
 - [11] H. A. Tieu, D. D. Joseph, and G. S. Beavers, *J. Fluid Mech.* **145**, 11 (1984).
 - [12] D. D. Joseph, *Fluid Dynamics of Viscoelastic Liquids* (Springer-Verlag, New York, 1990).
 - [13] G. Eitelberg, *Rheol. Acta* **22**, 131 (1983).
 - [14] G. Eitelberg, Ph.D. thesis, Universität Karlsruhe, 1984 (unpublished).
 - [15] J. Yoo, D. D. Joseph, and G. S. Beavers, *J. Fluid Mech.* **92**, 529 (1979).
 - [16] W. H. Press *et al.*, *Numerical Recipes in FORTRAN*, 2nd ed. (Cambridge University Press, Cambridge, 1992).
 - [17] H. D. Abarbanel, *Analysis of Observed Chaotic Data* (Springer-Verlag, New York, 1996).
 - [18] P. Bergé, Y. Pomeau, and C. Vidal, *Order within Chaos* (Hermann, Paris, 1984).
 - [19] R. L. Lewis, First Brands Corporation Report No. MSDS0069, 1993 (unpublished).